Chiral spin channels in curved graphene *pn* junctions

Dario Bercioux [1,2,*] Diego Frustaglia [3,†] and Alessandro De Martino [4,‡]
[1]*Donostia International Physics Center (DIPC), Manuel de Lardizbal 4, E-20018 San Sebastián, Spain*
[2]*IKERBASQUE, Basque Foundation for Science, Euskadi Plaza, 5, 48009 Bilbao, Spain*
[3]*Departamento de Física Aplicada II, Universidad de Sevilla, E-41012 Sevilla, Spain*
[4]*Department of Mathematics, City, University of London, London EC1V 0HB, United Kingdom*

(Received 10 March 2023; accepted 7 September 2023; published 20 September 2023)

We show that the chiral modes in circular graphene *pn* junctions provide an advantage for spin manipulation via spin-orbit coupling compared to semiconductor platforms. We derive the effective Hamiltonian for the spin dynamics of the junction's zero modes and calculate their quantum phases. We find a sweet spot in parameter space where the spin is fully in-plane and radially polarized for a given junction polarity. This represents a shortcut to singular spin configurations that would otherwise require spin-orbit coupling strengths beyond experimental reach.

DOI: 10.1103/PhysRevB.108.115140

I. INTRODUCTION

Graphene has attracted exceptional interest as a quantum material with Dirac cones at the Fermi energy and other unique electronic properties [1–3]. One appealing feature is the possibility of tuning electrostatically the charge carriers' polarity in *pn* junctions of linear [4–9] and circular shape [10–18]. The latter have been created by different means, such as the tip potential of a scanning tunneling microscope [10,14,16,18] or by placing impurities in the substrate [11,13]. In both approaches, experiments have shown that it is possible to single out and steer individual electronic eigenstates. Importantly, *pn* junctions are essential building blocks for graphene-based electron-optical elements and edge-state interferometers [14,19–21] also exploiting the so-called snake states [9,22,23].

The electronic spin degree of freedom is usually neglected in the study of graphene *pn* junctions because of the weak atomic spin-orbit coupling (SOC) of carbon [24–27]. However, theoretical predictions followed by experimental realizations proved that strong SOCs can be induced, e.g., by proximity with transition metal dichalcogenide (TMD) substrates [28–37]. These advances open the exciting possibility of including the spin functionality in graphene-based electron optics, with the further benefit that the versatility of *pn* junctions allows for the design of curved waveguides for spin and charge carriers. This is particularly interesting in view of the intense current theoretical and experimental research activity on the spin dynamics triggered by SOC in curved geometries [38–41]. The effects of SOC in graphene have been also investigated in other geometries [42–45].

In this article, we investigate circular *pn* junctions in the presence of (i) a perpendicular magnetic field, coupled to the electronic charge (developing Landau levels in the quantum Hall regime) and spin (through Zeeman coupling), and (ii) proximity-induced SOCs of different types. We provide the exact solution of graphene's Dirac equation for this system and formulate an effective one-dimensional (1D) model for the spin and angular dynamics of the states localized at the *pn* interface. This resembles the model for semiconductor rings subject to Rashba SOC (RSOC) [46], with a meaningful difference: the chiral nature of the propagating modes. We identify a remarkable sweet spot in the parameter space, where the spin eigenstates align locally with the effective magnetic field produced by the SOC. This point coincides with the Rabi condition for electronic spin resonance in a magnetic field and represents a shortcut to adiabatic spin dynamics unavailable in its semiconductor equivalent. We confirm this result within the original full model and propose a setup to identify this sweet spot via spin interferometry, opening a promising route to spin state manipulation in graphene.

The article is organized in the following way. In Sec. II, we introduce the model system. In Sec. III, we present a low-energy model for the system under investigation, where we show the presence of the sweet spot in the parameter space. In Sec. IV, we provide a proposal for an interferometric experiment to detect the presence of this sweet spot. We discuss in Sec. V the interpretation of the experimental proposal and its range of validity. Finally, in Sec. VI, we provide our conclusions. All the technical details are presented in the Supplemental Material (SM) [47].

II. MODEL

The low-energy model for graphene with proximity-induced SOCs reads

$$\mathcal{H} = \mathcal{H}_0 + \mathcal{H}_{\text{spin}}, \tag{1}$$

*dario.bercioux@dipc.org
†frustaglia@us.es
‡ademarti@city.ac.uk

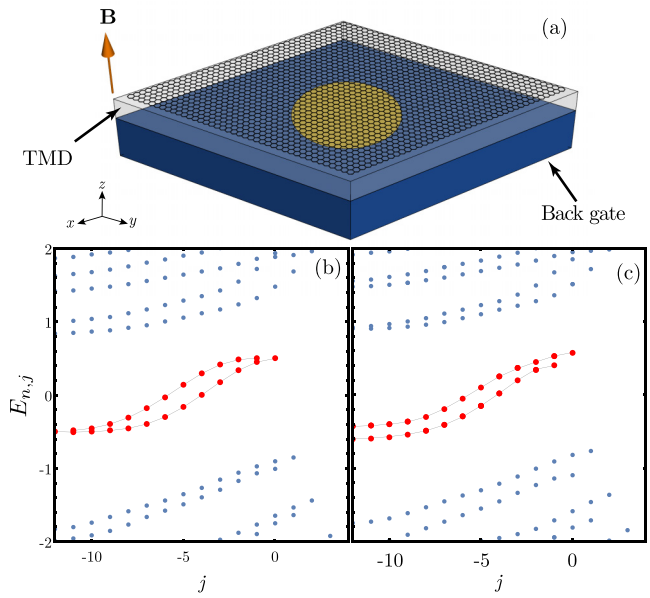

FIG. 1. (a) Sketch of the system, with p and n regions drawn in yellow and blue. (b) Energy spectrum versus angular momentum j for $V_0 = 0.51$, $\xi_0 = 5.1$, $\lambda_R = 0.5$, and $\lambda_Z = \lambda_{KM} = 0$. (c) Same as in (b) but for $\lambda_Z = 0.1$. In (b) and (c), the red dots highlight the zeroth Landau levels.

where $\mathcal{H}_0$ is the Dirac Hamiltonian in a perpendicular magnetic field

$$\mathcal{H}_0 = v_F(\tau\sigma_x\Pi_x + \sigma_y\Pi_y) + V, \tag{2}$$

with Fermi velocity v_F and kinetic momentum $\mathbf{\Pi} = -i\hbar\nabla + \frac{e}{c}\boldsymbol{A}$, with $\boldsymbol{A} = \frac{B}{2}(-y, x)$ in the symmetric gauge. Here, $\tau = \pm 1$ denotes the valley index and $\boldsymbol{\sigma} = (\sigma_x, \sigma_y)$ are Pauli matrices in sublattice space [3]. The potential

$$V(r) = V_0\,\mathrm{sgn}(R - r) \tag{3}$$

defines a circular pn junction of radius R, with a p-doped region for $r < R$ (the "dot") and an n-doped region for $r > R$. The system is sketched in Fig. 1(a). The spin-dependent part $\mathcal{H}_{spin} = \mathcal{H}_Z + \mathcal{H}_R + \mathcal{H}_{KM} + \mathcal{H}_{VZ}$ includes both Zeeman and SOCs terms [28,29,48]:

$$\mathcal{H}_Z = \lambda_Z s_z, \tag{4a}$$

$$\mathcal{H}_R = \frac{\lambda_R}{2}(\tau\sigma_x s_y - \sigma_y s_x), \tag{4b}$$

$$\mathcal{H}_{KM} = \lambda_{KM}\tau\sigma_z s_z, \tag{4c}$$

$$\mathcal{H}_{VZ} = \lambda_{VZ}\tau s_z. \tag{4d}$$

Here $\lambda_Z = \frac{g_s\mu_B}{2}B$ and $\boldsymbol{s} = (s_x, s_y)$ denotes the Pauli matrices in spin space. The terms $\mathcal{H}_R$, $\mathcal{H}_{KM}$, and $\mathcal{H}_{VZ}$ are the Rashba, Kane-Mele, and valley-Zeeman SOC, respectively [24,26,49]. Precise estimates for the SOCs depend on the specific heterostructure, e.g., the relative orientation between graphene and substrate [35,36]. The RSOC and the VZSOC range from few hundredths of meV up to few meV, while the KMSOC is typically much smaller [35,37]. We are mainly concerned with the effects of the Zeeman and RSOC terms. The valley-Zeeman term can be included by means of a valley-dependent shift of the Zeeman coupling and will be considered separately in the Discussion section below. For $\lambda_{VZ} = 0$, the valley degree of freedom just leads to a degeneracy factor, so we can focus on a single valley and set $\tau = +1$. Throughout this paper, we measure lengths in units of magnetic length $\ell_B = \sqrt{\hbar c/eB} = 25.65\ \mathrm{nm}/\sqrt{B[\mathrm{T}]}$ and energies in units of cyclotron energy $\hbar\omega_c = \hbar v_F/\ell_B \approx 26\ \mathrm{meV}\sqrt{B[\mathrm{T}]}$ and assume a typical field $B \sim 1$ T [37].

In this model, the wave function is a four-component spinor $\Psi^T = (\Psi_{A\uparrow}, \Psi_{B\uparrow}, \Psi_{A\downarrow}, \Psi_{B\downarrow})$. The Hamiltonian $\mathcal{H}$ commutes with the total angular momentum $J = L_z + \frac{1}{2}(\sigma_z + s_z)$, with $L_z = -i\partial_\theta$ the orbital angular momentum; hence its eigenstates $\Psi_j(\mathbf{r})$, expressed in terms of confluent hypergeometric functions [47,50–52], can be labeled by an integer $j \in \mathbb{Z}$. The spectrum is illustrated in Figs. 1(b) and 1(c). In particular, we find two "zero-energy" Landau levels (LLs), the "top" (T) and "bottom" (B) zero modes, highlighted in red in the figures. In the absence of SOCs, they have zero energy for $V_0 = 0$, but develop a dispersion in j for finite V_0 [22,47]. Their energy at $j = 0$ and at $j \ll -1$ approaches the value of the potential $V(r)$ inside and outside the dot, respectively; see Fig. 1(b). In the presence of RSOC, the two modes acquire a spin splitting, similar to the case of a two-dimensional electron gas (2DEG) [27,53]. A finite Zeeman coupling produces an additional vertical splitting—see Fig. 1(c). We present in the SM [47] the exact solution of the model (1), including a detailed analysis of the spin splitting as a function of λ_R.

III. EFFECTIVE 1D MODEL

In order to describe the low-energy physics around the Fermi energy (set at the charge neutrality point, $E_F = 0$), we introduce an effective 1D Hamiltonian for the zero modes localized at the pn interface. We follow an analogous derivation for a semiconductor ring with RSOC [54]; see the SM [47] for details. We first perform a unitary transformation, $\mathcal{H} \to \tilde{\mathcal{H}} = U\mathcal{H}U^{-1}$, with $U = e^{i\frac{\sigma_z}{2}(\theta+\frac{\pi}{2})}e^{i\frac{s_z}{2}\theta}$. In this rotating frame, we factorize the wave function as $\tilde{\Psi} = \tilde{\psi}_0(r)\tilde{\chi}(\theta)$, where $\tilde{\psi}_0(r)$ is the sublattice spinor for the (spin degenerate) zero mode of the radial part of $\tilde{\mathcal{H}}_0$, and $\tilde{\chi}(\theta)$ is a spinor in spin space, containing the angular dependence. The projection of $\tilde{\mathcal{H}}$ onto the zero mode $\tilde{\psi}_0(r)$ leads to the effective 1D Hamiltonian controlling the dynamics of $\tilde{\chi}(\theta)$:

$$\tilde{\mathcal{H}}_{eff} = \omega_0(L_z + \Phi) + \left(\omega_Z - \frac{\omega_0}{2}\right)s_z - \omega_R s_x. \tag{5}$$

The frequencies in Eq. (5) are defined by

$$\omega_0 = \left\langle\frac{\sigma_x}{r}\right\rangle_0, \tag{6a}$$

$$\omega_Z = \lambda_Z + \lambda_{KM}\langle\sigma_z\rangle_0, \tag{6b}$$

$$\omega_R = \frac{\lambda_R}{2}\langle\sigma_x\rangle_0, \tag{6c}$$

where $\langle\ldots\rangle_0$ denotes the (radial) expectation value in the state $\tilde{\psi}_0(r)$. (We note that σ_x is the azimuthal component of the velocity operator in the rotating frame.) The parameter $\Phi \approx \xi_0 = B\pi R^2/\Phi_0$ denotes approximately the magnetic flux through the dot in units of the flux quantum Φ_0. Since $\tilde{\mathcal{H}}_{spin}$ is treated perturbatively, this projection is justified as long as $\hbar\omega_c$ is much larger than the Zeeman and SOCs. The Hamiltonian (5) describes a 1D spinful chiral mode propagating along

the curved *pn* interface, with angular velocity controlled by the gate voltage difference across the junction. Importantly, the polarity of the junction determines the signs of ω_0 and ω_R [55]. For $V_0 > 0$ both are positive. Inverting the polarity, $V_0 \to -V_0$, reverses the propagation direction, changing both signs. This feature has crucial implications for the experimental setup discussed below.

Diagonalizing $\tilde{\mathcal{H}}_{\rm eff}$, we obtain the eigenvalues

$$E_{m,\pm} = \omega_0(m+\Phi) \pm \sqrt{\left(\omega_Z - \frac{\omega_0}{2}\right)^2 + \omega_R^2}, \tag{7}$$

where $m \in \mathbb{Z}$ under periodic boundary conditions. This formula predicts a linear dependence of the energy on m, which we observe in the exact solution close to zero energy, and provides an approximate analytical expression for the slope of the dispersion. The corresponding eigenstates are

$$\tilde{\chi}_{m,+} = \frac{e^{im\theta}}{\sqrt{2\pi}} \begin{pmatrix} \cos\frac{\gamma}{2} \\ -\sin\frac{\gamma}{2} \end{pmatrix}, \tag{8a}$$

$$\chi_{m,-} = \frac{e^{im\theta}}{\sqrt{2\pi}} \begin{pmatrix} \sin\frac{\gamma}{2} \\ \cos\frac{\gamma}{2} \end{pmatrix}, \tag{8b}$$

where

$$e^{i\gamma} = \frac{\omega_Z - \frac{\omega_0}{2} + i\omega_R}{\sqrt{\left(\omega_Z - \frac{\omega_0}{2}\right)^2 + \omega_R^2}}. \tag{9}$$

We find a sweet spot for $\omega_Z = \frac{\omega_0}{2}$ ($\gamma = \frac{\pi}{2}$), where the spin eigenstates (8) point along the radial direction in the xy plane for any value of ω_R. This situation is remarkable. It recalls the Rabi condition for spin resonance in the rotating wave approximation (RWA), with the difference that there is no Bloch-Siegert shift [56] as a function of the driving amplitude (represented by ω_R): here, the RWA is exact. Notice that an inversion of the junction polarity, changing the chirality of the propagating spin channels ($\omega_0 \to -\omega_0$), would take the system off resonance. This is in sharp contrast to the case of semiconductor-based Rashba rings [46,57], where counter-propagating channels coexist, and a full in-plane alignment of the spinors is only achieved in the adiabatic limit of very large RSOC ($\omega_R \gg \omega_0$) [46].

The resonance condition, exact in the projected model (5), holds with excellent accuracy also in the full model (1). This is shown in Fig. 2, where for simplicity we set $\lambda_{KM} = 0$. Here, we define the angular frequency ω_0 as the expectation value $\langle \sigma_x/r \rangle_{\lambda_R=0}$ on the j state closest to zero energy. From Fig. 2(a), we can see that ω_0 decreases as a function of the radius R and presents a staircase behavior due to the discreteness of j. In Figs. 2(b)–2(d), we show the expectation values of the perpendicular and radial components of the spin, s_z and s_r, in the top and bottom j states closest to zero energy for different sets of parameters. We observe that, at the value of ξ_0 where the resonance condition $\omega_Z = \frac{\omega_0}{2}$ is realized, $\langle s_z \rangle$ is almost zero, whereas $\langle s_r \rangle$ is close to 1. The results in Fig. 2 show an excellent agreement between the prediction of the projected model and the full solution. In particular, they confirm that the resonance condition is independent of the RSOC. The small discrepancies are due to the coupling of the zero modes to the higher LLs via the RSOC, neglected in the projected model.

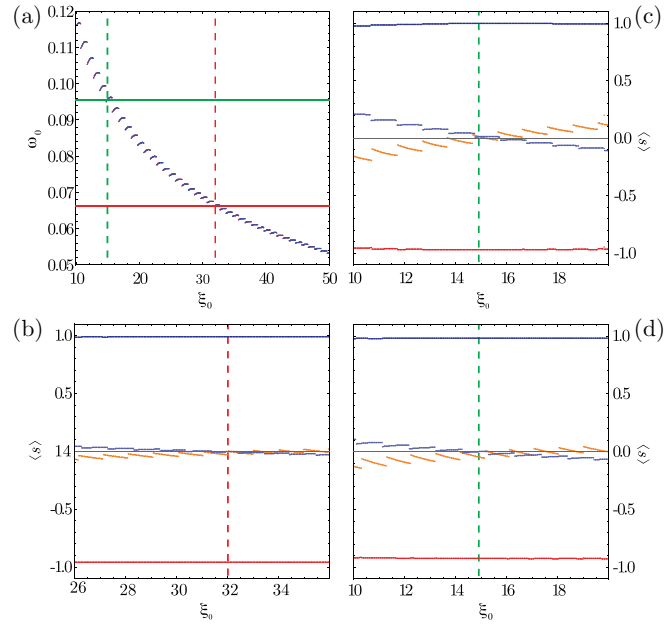

FIG. 2. Sweet spot identification in the full model. (a) The angular frequency ω_0 as a function of $\xi_0 = R^2/2\ell_B^2$, at a fixed magnetic field. The green and red horizontal lines describe two representative values of $2\omega_Z$ and the vertical dashed lines the corresponding values of ξ_0 at which the resonance condition $2\omega_Z = \omega_0$ is realized. (b)–(d) The exact expectation values of the radial and perpendicular spin components in the top and bottom modes as a function of ξ_0, for $\lambda_Z = 0.047$ and $\lambda_R = 0.2$ in (b) and for $\lambda_Z = 0.033$ and $\lambda_R = 0.2, 0.3$ in (c) and (d), respectively. In (b)–(d), the top curve shows $\langle s_r \rangle_B$, the bottom one $\langle s_r \rangle_T$, and the two central ones $\langle s_z \rangle_T$ and $\langle s_z \rangle_B$. In all the panels, $V_0 = 0.51$.

We present additional results, including the effect of λ_{KM}, in the SM [47].

IV. EXPERIMENTAL PROPOSAL

We propose two setups based on linear and circular *pn* junctions to implement interferometric circuits for spin carriers. Thanks to the chiral nature of the propagating channels, we find that, depending on the junction polarity, the interferometers respond differently to the Zeeman coupling ω_Z (assuming $\lambda_{KM} = 0$ for simplicity), making possible a unique geometric characterization of the propagating spin states.

Figure 3 depicts the circuits' architecture built upon n [Fig. 3(a)] and p [Fig. 3(b)] dots. Contact 1 at voltage V is the carrier source, while the grounded contacts 2 and 3 act as drains. The grounded contact 4 contributes with an empty channel. Importantly, either setup can be turned into the other by simply inverting the *pn* polarity, relabeling the contacts, and swapping voltages, meaning that a single sample could realize both interferometers in the laboratory.

Carriers injected from contact 1 propagate along a linear *pn* junction. Traveling toward contact 2, they can enter the circular *pn* junction with probability $0 < \tau_1 < 1$, from which they can escape at the opposite end towards contact 3 with probability $0 < \tau_2 < 1$. The tunnel barriers τ_1 and τ_2 operate as beam splitters (BSs) for the chiral modes. Their spin-dependent probability amplitudes are determined

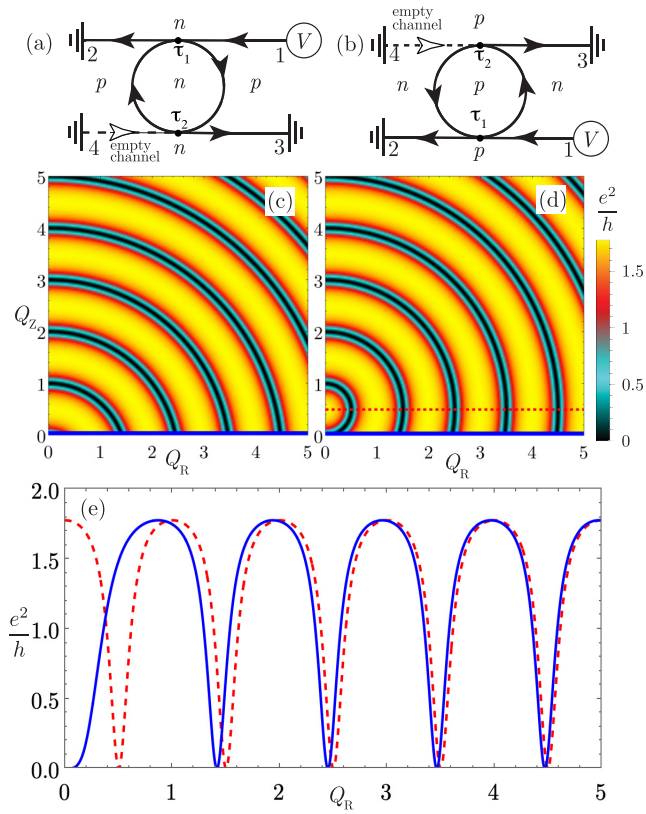

FIG. 3. (a) Circuit's architecture with an n-doped dot. (b) The same as in (a), but with opposite junctions' polarity. (c), (d) Differential conductance G_{21} for the circuits in (a) and (b), respectively, as a function of the dimensionless Rashba and Zeeman coupling strengths. (e) Cut of the differential conductance for the cases in (c) and (d) with $Q_Z = 0$ (blue line) and for the case in (d) with $Q_Z = 1/2$ (red dashed line).

by projecting the propagating spin modes on the local basis [47].

We calculate the quantum conductance G_{21} from contact 1 to contact 2 for the zero modes following the Landauer-Büttiker approach [58,59]. (By unitarity, $G_{21} + G_{31} = 2e^2/h$, since we are considering a single valley.) Obtaining the quantum transmission requires the combination of the BS scattering matrices [59], taking into account the spin-dependent phases $m\pi$ gathered by the carriers propagating between the tunnel barriers along the circular junction [47]. These phases are obtained by setting $E_{m,s} = 0$ in Eq. (7), where m is not necessarily an integer for open pn junctions, since periodic boundary conditions do not apply in the presence of contact leads. Figures 3(c)–3(e) summarize our main results. We plot the conductance G_{21} for the two opposite junction polarities, as a function of dimensionless Rashba $Q_R = \omega_R/\omega_0$ and Zeeman $Q_Z = \omega_Z/\omega_0$ coupling strengths. Without loss of generality, we set $\tau_1 = \tau_2 = 1/2$ (50% BSs) and $\Phi \in \mathbb{N}$. Other settings can modify the relative amplitudes and phases of the patterns, but their general composition remains the same. We observe that the patterns in Figs. 3(c) and 3(d) differ by a relative $\Delta Q_Z = 1$ shift along the Zeeman axis. This shift reveals significant information on the spin-state geometry of propagating channels, as explained below.

In Fig. 3(e) we plot G_{21} for $Q_Z = 0$ (solid line) and $Q_Z = 1/2$ (dashed line). For $Q_Z = 0$, the result holds for both n and p polarities. Here we find quasiperiodic oscillations as a function of Q_R, which tend to be periodic for $Q_R \gg 1$. This limit corresponds to the regime of adiabatic spin dynamics, where the local spin quantization axis is expected to point along the radial Rashba field with $\gamma \to \pi/2$ in Eq. (8). Moreover, after a round trip around the dot, the spin carriers collect a geometric phase $\varphi_g = -\Omega/2$, with $\Omega = 2\pi(1 - \cos\gamma)$ the solid angle subtended by the spin states on the Bloch sphere. In the adiabatic limit, one finds $\varphi_g \to -\pi$. Similar results have been reported for semiconductor Rashba rings [46,57].

The two polarities respond very differently to Q_Z. For the n dot [see Eq. (9) and Fig. 3(c)], we find that Q_Z acts to the detriment of in-plane spinor polarization, which still requires large RSOC intensities Q_R. On the contrary, for the p dot [see Eq. (9) and Figs. 3(d) and 3(e)], at the sweet spot $Q_Z = 1/2$ we find perfectly periodic oscillations corresponding to fully in-plane spin states ($\gamma = \pi/2$) regardless of the RSOC intensity, picking up a geometric phase $\varphi_g = -\pi$.

V. DISCUSSION

All relevant features of Fig. 3(d) are captured by a low-order semiclassical expansion of the conductance in terms of Feynman paths corresponding to single windings around the p dot [47]. In this approximation, we find

$$G_{21} \approx 1 + \cos\phi_{AB}\cos\phi_S, \tag{10}$$

with

$$\phi_{AB} = 2\pi\Phi, \tag{11a}$$

$$\phi_S = 2\pi\sqrt{\left(Q_Z - \frac{1}{2}\right)^2 + Q_R^2}, \tag{11b}$$

where ϕ_{AB} and ϕ_S are independent phase contributions originating in the orbital and spin degrees of freedom, respectively. Equation (10) reproduces well the pattern of Fig. 3(d) showing circular wave fronts centered at $Q_R = 0$ and $Q_Z = 1/2$. For $Q_Z = 0$, we find from Eq. (10) that $\phi_S = 2\pi Q_R \sin\gamma - \pi\cos\gamma = 2\pi Q_R \sin\gamma - (\pi + \varphi_g)$. This phase reduces to $\phi_S \approx 2\pi Q_R$ in the adiabatic limit $Q_R \gg 1$, leading to periodic oscillations of G_{21} as a function of Q_R. Thus a strong RSOC drives the spin eigenstates to be in-plane, such that $\gamma \to \pi/2$ and $\varphi_g \to -\pi$. The physical realization of this formal limit is difficult in the laboratory due to the required field intensities. Alternatively, we find here a shortcut by setting $Q_Z = 1/2$. In this sweet spot, the spin phase contribution reduces exactly to $\phi_S = 2\pi Q_R$ even for weak RSOC fields, which assures in-plane spin eigenstates that introduce a π phase shift of purely geometric origin.

We emphasize that this precise characterization of the propagating spin channels boils down to their chiral nature, in contrast to the case of semiconductor Rashba rings, where counterpropagating modes coexist [46,57,60]. The chirality also protects the sweet spot from the effect of random impurities. Moreover, we expect that small deviations from a perfectly circular shape breaking the rotational symmetry might induce small oscillations of the out-of-plane component

of the spin and thus blur the sweet spot, but will not qualitatively alter the physics discussed here [61].

Finally, we briefly address the effect of the VZSOC. In the effective model (5), it leads to a valley-dependent shift $\omega_Z \to \omega_Z + \tau\lambda_{VZ}$. Hence, at $\omega_Z = \omega_0/2$, the spin states (8) will have a residual out-of-plane component, opposite at the two valleys. The valley-resolved conductances will be periodic functions of Q_R only for $\lambda_R \gg \lambda_{VZ}$ [47]; see Eqs. (10) and (11b). The selection of substrates inducing the weakest possible VZSOC [35,36] is thus essential to observing the effects described in this work.

VI. CONCLUSIONS

We have shown that the chiral spin channels in curved graphene *pn* junctions with proximitized SOCs can be precisely characterized and controlled. We uncovered a sweet spot in the parameter space enabling an efficient manipulation of spin-state configurations without requiring a strong RSOC, which is difficult to achieve experimentally. This opens up new possibilities for exploring quantum-state geometry and advancing spintronics in graphene. Curved *pn* junctions thus offer a versatile platform for investigating spin dynamics phenomena induced by SOCs, providing an alternative to traditional semiconductor systems.

ACKNOWLEDGMENTS

We thank R. Egger and K. Richter for helpful comments on the manuscript. D.B. acknowledges the support from the Spanish MICINN-AEI through Project No. PID2020-120614GB-I00 (ENACT), the Transnational Common Laboratory *Quantum – ChemPhys*, the financial support received from the IKUR Strategy under the collaboration agreement between Ikerbasque Foundation and DIPC on behalf of the Department of Education of the Basque Government and the Gipuzkoa Provincial Council within the QUAN-000021-01 project. D.F. acknowledges support from the Spanish MICINN-AEI through Project No. PID2021-127250NB-I00 (e-QSG) and from the Andalusian Government through PAIDI 2020 Project No. P20-00548 and FEDER Project No. US-1380932.

[1] K. S. Novoselov, A. K. Geim, S. V. Morozov, D. Jiang, Y. Zhang, S. V. Dubonos, I. V. Grigorieva, and A. A. Firsov, Electric field effect in atomically thin carbon films, Science **306**, 666 (2004).

[2] K. S. Novoselov, A. Geim, S. V. Morozov, D. Jiang, M. I. Katsnelson, I. V. Grigorieva, S. V. Dubonos, and A. A. Firsov, Two-dimensional gas of massless Dirac fermions in graphene, Nature (London) **438**, 197 (2005).

[3] A. H. Castro Neto, F. Guinea, N. M. R. Peres, K. S. Novoselov, and A. K. Geim, The electronic properties of graphene, Rev. Mod. Phys. **81**, 109 (2009).

[4] D. A. Abanin and L. S. Levitov, Quantized transport in graphene *p-n* junctions in a magnetic field, Science **317**, 641 (2007).

[5] J. R. Williams, L. DiCarlo, and C. M. Marcus, Quantum Hall effect in a gate-controlled *p-n* junction of graphene, Science **317**, 638 (2007).

[6] J. R. Williams, T. Low, M. S. Lundstrom, and C. M. Marcus, Gate-controlled guiding of electrons in graphene, Nat. Nanotechnol. **6**, 222 (2011).

[7] J. R. Williams and C. M. Marcus, Snake States along Graphene *p-n* Junctions, Phys. Rev. Lett. **107**, 046602 (2011).

[8] B. Özyilmaz, P. Jarillo-Herrero, D. Efetov, D. A. Abanin, L. S. Levitov, and P. Kim, Electronic Transport and Quantum Hall Effect in Bipolar Graphene *p-n-p* Junctions, Phys. Rev. Lett. **99**, 166804 (2007).

[9] P. Rickhaus, P. Makk, M.-H. Liu, E. Tóvári, M. Weiss, R. Maurand, K. Richter, and C. Schönenberger, Snake trajectories in ultraclean graphene *p-n* junctions, Nat. Commun. **6**, 6470 (2015).

[10] N. M. Freitag, L. A. Chizhova, P. Nemes-Incze, C. R. Woods, R. V. Gorbachev, Y. Cao, A. K. Geim, K. S. Novoselov, J. Burgdörfer, F. Libisch, and M. Morgenstern, Electrostatically confined monolayer graphene quantum dots with orbital and valley splittings, Nano Lett. **16**, 5798 (2016).

[11] Y. Zhao, J. Wyrick, F. D. Natterer, J. F. Rodriguez-Nieva, C. Lewandowski, K. Watanabe, T. Taniguchi, L. S. Levitov, N. B. Zhitenev, and J. A. Stroscio, Creating and probing electron whispering-gallery modes in graphene, Science **348**, 672 (2015).

[12] J. F. Rodriguez-Nieva and L. S. Levitov, Berry phase jumps and giant nonreciprocity in Dirac quantum dots, Phys. Rev. B **94**, 235406 (2016).

[13] F. Ghahari, D. Walkup, C. Gutiérrez, J. F. Rodriguez-Nieva, Y. Zhao, J. Wyrick, F. D. Natterer, W. G. Cullen, K. Watanabe, T. Taniguchi, L. S. Levitov, N. B. Zhitenev, and J. A. Stroscio, An on/off Berry phase switch in circular graphene resonators, Science **356**, 845 (2017).

[14] Y. Jiang, J. Mao, D. Moldovan, M. R. Masir, G. Li, K. Watanabe, T. Taniguchi, F. M. Peeters, and E. Y. Andrei, Tuning a circular *p-n* junction in graphene from quantum confinement to optical guiding, Nat. Nanotechnol. **12**, 1045 (2017).

[15] C. Gutiérrez, D. Walkup, F. Ghahari, C. Lewandowski, J. F. Rodriguez-Nieva, K. Watanabe, T. Taniguchi, L. S. Levitov, N. B. Zhitenev, and J. A. Stroscio, Interaction-driven quantum Hall wedding cake-like structures in graphene quantum dots, Science **361**, 789 (2018).

[16] B. Brun, N. Moreau, S. Somanchi, V.-H. Nguyen, K. Watanabe, T. Taniguchi, J.-C. Charlier, C. Stampfer, and B. Hackens, Imaging Dirac fermions flow through a circular Veselago lens, Phys. Rev. B **100**, 041401(R) (2019).

[17] Y.-N. Ren, Q. Cheng, S.-Y. Li, C. Yan, Y.-W. Liu, K. Lv, M.-H. Zhang, Q.-F. Sun, and L. He, Spatial and magnetic confinement of massless Dirac fermions, Phys. Rev. B **104**, L161408 (2021).

[18] B. Brun, V.-H. Nguyen, N. Moreau, S. Somanchi, K. Watanabe, T. Taniguchi, J.-C. Charlier, C. Stampfer, and B. Hackens, Graphene whisperitronics: Transducing whispering gallery modes into electronic transport, Nano Lett. **22**, 128 (2022).

[19] A. Mreńca-Kolasińska, S. Heun, and B. Szafran, Aharonov-Bohm interferometer based on *n-p* junctions in graphene nanoribbons, Phys. Rev. B **93**, 125411 (2016).

[20] M. Jo, P. Brasseur, A. Assouline, G. Fleury, H.-S. Sim, K. Watanabe, T. Taniguchi, W. Dumnernpanich, P. Roche, D. C. Glattli, N. Kumada, F. D. Parmentier, and P. Roulleau, Quantum Hall Valley Splitters and a Tunable Mach-Zehnder Interferometer in Graphene, Phys. Rev. Lett. **126**, 146803 (2021).

[21] I. M. Flór, A. Lacerda-Santos, G. Fleury, P. Roulleau, and X. Waintal, Positioning of edge states in a quantum Hall graphene *pn* junction, Phys. Rev. B **105**, L241409 (2022).

[22] L. Cohnitz, A. De Martino, W. Häusler, and R. Egger, Chiral interface states in graphene *p-n* junctions, Phys. Rev. B **94**, 165443 (2016).

[23] P. Makk, C. Handschin, E. Tóvári, K. Watanabe, T. Taniguchi, K. Richter, M.-H. Liu, and C. Schönenberger, Coexistence of classical snake states and Aharonov-Bohm oscillations along graphene *p-n* junctions, Phys. Rev. B **98**, 035413 (2018).

[24] D. Huertas-Hernando, F. Guinea, and A. Brataas, Spin-orbit coupling in curved graphene, fullerenes, nanotubes, and nanotube caps, Phys. Rev. B **74**, 155426 (2006).

[25] J. C. Boettger and S. B. Trickey, First-principles calculation of the spin-orbit splitting in graphene, Phys. Rev. B **75**, 121402(R) (2007).

[26] M. Gmitra, S. Konschuh, C. Ertler, C. Ambrosch-Draxl, and J. Fabian, Band-structure topologies of graphene: Spin-orbit coupling effects from first principles, Phys. Rev. B **80**, 235431 (2009).

[27] D. Bercioux and P. Lucignano, Quantum transport in Rashba spin–orbit materials: A review, Rep. Prog. Phys. **78**, 106001 (2015).

[28] M. Gmitra and J. Fabian, Graphene on transition-metal dichalcogenides: A platform for proximity spin-orbit physics and optospintronics, Phys. Rev. B **92**, 155403 (2015).

[29] M. Gmitra, D. Kochan, P. Högl, and J. Fabian, Trivial and inverted Dirac bands and the emergence of quantum spin Hall states in graphene on transition-metal dichalcogenides, Phys. Rev. B **93**, 155104 (2016).

[30] Z. Wang, D. Ki, H. Chen, H. Berger, A. H. MacDonald, and A. F. Morpurgo, Strong interface-induced spin-orbit interaction in graphene on WS_2, Nat. Commun. **6**, 8339 (2015).

[31] Z. Wang, D.-K. Ki, J. Y. Khoo, D. Mauro, H. Berger, L. S. Levitov, and A. F. Morpurgo, Origin and Magnitude of 'Designer' Spin-Orbit Interaction in Graphene on Semiconducting Transition Metal Dichalcogenides, Phys. Rev. X **6**, 041020 (2016).

[32] T. Wakamura, N. J. Wu, A. D. Chepelianskii, S. Guéron, M. Och, M. Ferrier, T. Taniguchi, K. Watanabe, C. Mattevi, and H. Bouchiat, Spin-Orbit-Enhanced Robustness of Supercurrent in Graphene/WS_2 Josephson Junctions, Phys. Rev. Lett. **125**, 266801 (2020).

[33] T. Wakamura, S. Guéron, and H. Bouchiat, Novel transport phenomena in graphene induced by strong spin-orbit interaction, C. R. Phys. **22**, 145 (2021).

[34] D. Wang, M. Karaki, N. Mazzucca, H. Tian, G. Cao, C. N. Lau, Y.-M. Lu, M. Bockrath, K. Watanabe, and T. Taniguchi, Spin-orbit coupling and interactions in quantum Hall states of graphene/WSe_2 heterobilayers, Phys. Rev. B **104**, L201301 (2021).

[35] T. Naimer, K. Zollner, M. Gmitra, and J. Fabian, Twist-angle dependent proximity induced spin-orbit coupling in graphene/transition metal dichalcogenide heterostructures, Phys. Rev. B **104**, 195156 (2021).

[36] T. Naimer and J. Fabian, Twist-angle dependent proximity induced spin-orbit coupling in graphene/topological insulator heterostructures, Phys. Rev. B **107**, 195144 (2023).

[37] P. Tiwari, M. K. Jat, A. Udupa, D. S. Narang, K. Watanabe, T. Taniguchi, D. Sen, and A. Bid, Experimental observation of spin-split energy dispersion in high-mobility single-layer graphene/WSe_2 heterostructures, npj 2D Mater. Appl. **6**, 68 (2022).

[38] K. S. Das, D. Makarov, P. Gentile, M. Cuoco, B. J. van Wees, C. Ortix, and I. J. Vera-Marun, Independent geometrical control of spin and charge resistances in curved spintronics, Nano Lett. **19**, 6839 (2019).

[39] D. Frustaglia and J. Nitta, Geometric spin phases in Aharonov-Casher interference, Solid State Commun. **311**, 113864 (2020).

[40] R. Streubel, E. Y. Tsymbal, and P. Fischer, Magnetism in curved geometries, J. Appl. Phys. **129**, 210902 (2021).

[41] P. Gentile, M. Cuoco, O. M. Volkov, Z.-J. Ying, I. J. Vera-Marun, D. Makarov, and C. Ortix, Electronic materials with nanoscale curved geometries, Nat. Electron. **5**, 551 (2022).

[42] M. Zarea and N. Sandler, Rashba spin-orbit interaction in graphene and zigzag nanoribbons, Phys. Rev. B **79**, 165442 (2009).

[43] A. De Martino, A. Hütten, and R. Egger, Landau levels, edge states, and strained magnetic waveguides in graphene monolayers with enhanced spin-orbit interaction, Phys. Rev. B **84**, 155420 (2011).

[44] L. Lenz and D. Bercioux, Dirac-Weyl electrons in a periodic spin-orbit potential, Europhys. Lett. **96**, 27006 (2011).

[45] L. Lenz, D. F. Urban, and D. Bercioux, Rashba spin-orbit interaction in graphene armchair nanoribbons, Eur. Phys. J. B **86**, 502 (2013).

[46] D. Frustaglia and K. Richter, Spin interference effects in ring conductors subject to Rashba coupling, Phys. Rev. B **69**, 235310 (2004).

[47] See Supplemental Material at http://link.aps.org/supplemental/10.1103/PhysRevB.108.115140 for details of the full model and its solution in the uniform case and for the junction, detailed derivation of the effective 1D model, additional cases for the Rabi condition, and the details for the construction of the S matrix and its first order expansion.

[48] T. Frank and J. Fabian, Landau levels in spin-orbit coupling proximitized graphene: Bulk states, Phys. Rev. B **102**, 165416 (2020).

[49] C. L. Kane and E. J. Mele, Z_2 Topological Order and the Quantum Spin Hall Effect, Phys. Rev. Lett. **95**, 146802 (2005).

[50] *NIST Handbook of Mathematical Functions*, edited by F. W. Olver, D. W. Lozier, R. F. Boisvert, and C. W. Clark (Cambridge University Press, Cambridge, UK, 2010).

[51] A. De Martino, L. Dell'Anna, and R. Egger, Magnetic Confinement of Massless Dirac Fermions in Graphene, Phys. Rev. Lett. **98**, 066802 (2007).

[52] A. De Martino and R. Egger, On the spectrum of a magnetic quantum dot in graphene, Semicond. Sci. Technol. **25**, 034006 (2010).

[53] D. Bercioux and A. De Martino, Spin-orbit interaction and snake states in a graphene *p-n* junction, Phys. Rev. B **100**, 115407 (2019).

[54] F. E. Meijer, A. F. Morpurgo, and T. M. Klapwijk, One-dimensional ring in the presence of Rashba spin-orbit

interaction: Derivation of the correct Hamiltonian, Phys. Rev. B **66**, 033107 (2002).

[55] We note that the signs of ω_0 and ω_R are independent of the valley index.

[56] F. Bloch and A. Siegert, Magnetic Resonance for Nonrotating Fields, Phys. Rev. **57**, 522 (1940).

[57] F. Nagasawa, J. Takagi, Y. Kunihashi, M. Kohda, and J. Nitta, Experimental Demonstration of Spin Geometric Phase: Radius Dependence of Time-Reversal Aharonov-Casher Oscillations, Phys. Rev. Lett. **108**, 086801 (2012).

[58] Y. Imry, *Introduction to Mesoscopic Physics* (Oxford University Press, Oxford, 1997), Chap. 5.

[59] S. Datta, *Electronic Transport in Mesoscopic Systems*, Cambridge Studies in Semiconductor Physics and Microelectronic Engineering (Cambridge University Press, Cambridge, UK, 1995).

[60] F. Nagasawa, D. Frustaglia, H. Saarikoski, K. Richter, and J. Nitta, Control of the spin geometric phase in semiconductor quantum rings, Nat. Commun. **4**, 2526 (2013).

[61] Z.-J. Ying, P. Gentile, C. Ortix, and M. Cuoco, Designing electron spin textures and spin interferometers by shape deformations, Phys. Rev. B **94**, 081406(R) (2016).